The Astrophysical Journal Supplement Series, 256:21 (34pp), 2021 September https://doi.org/10.3847/1538-4365/ac0dc6

The XMM-SERVS Survey: XMM-Newton Point-source Catalogs for the W-CDF-S and ELAIS-S1 Fields

Qingling Ni[1,2], W. N. Brandt[1,2,3], Chien-Ting Chen[4], Bin Luo[5,6], Kristina Nyland[7], Guang Yang[8,9], Fan Zou[1,2], James Aird[10], David M. Alexander[11], Franz Erik Bauer[12,13,14], Mark Lacy[15], Bret D. Lehmer[16], Labani Mallick[17], Mara Salvato[18], Donald P. Schneider[1,2], Paolo Tozzi[19], Iris Traulsen[20], Mattia Vaccari[21,22], Cristian Vignali[23,24], Fabio Vito[25], Yongquan Xue[26,27], Manda Banerji[28], Kate Chow[29], Andrea Comastri[24], Agnese Del Moro[30], Roberto Gilli[24], James Mullaney[31], Maurizio Paolillo[32,33,34], Axel Schwope[20], Ohad Shemmer[35], Mouyuan Sun[36], John D. Timlin III[1,2], and Jonathan R. Trump[37]

[1] Department of Astronomy and Astrophysics, 525 Davey Lab, The Pennsylvania State University, University Park, PA 16802, USA; qingling1001@gmail.com
[2] Institute for Gravitation and the Cosmos, The Pennsylvania State University, University Park, PA 16802, USA
[3] Department of Physics, 104 Davey Laboratory, The Pennsylvania State University, University Park, PA 16802, USA
[4] Marshall Space Flight Center, Huntsville, AL 35811, USA
[5] School of Astronomy and Space Science, Nanjing University, Nanjing, Jiangsu 210093, People's Republic of China
[6] Key Laboratory of Modern Astronomy and Astrophysics (Nanjing University), Ministry of Education, Nanjing, Jiangsu 210093, People's Republic of China
[7] National Research Council, resident at the U.S. Naval Research Laboratory, 4555 Overlook Avenue SW, Washington, DC 20375, USA
[8] Department of Physics and Astronomy, Texas A&M University, College Station, TX 77843-4242, USA
[9] George P. and Cynthia Woods Mitchell Institute for Fundamental Physics and Astronomy, Texas A&M University, College Station, TX 77843-4242, USA
[10] Institute for Astronomy, University of Edinburgh, Royal Observatory, Edinburgh EH9 3HJ, UK
[11] Centre for Extragalactic Astronomy, Department of Physics, Durham University, Durham DH1 3LE, UK
[12] Instituto de Astrofísica and Centro de Astroingeniería, Facultad de Física, Pontificia Universidad Católica de Chile, Casilla 306, Santiago 22, Chile
[13] Millennium Institute of Astrophysics, Nuncio Monseñor Sótero Sanz 100, Of 104, Providencia, Santiago, Chile
[14] Space Science Institute, 4750 Walnut Street, Suite 205, Boulder, CO 80301, USA
[15] National Radio Astronomy Observatory, 520 Edgemont Road, Charlottesville, VA 22903, USA
[16] Department of Physics, University of Arkansas, 226 Physics Building, 825 West Dickson Street, Fayetteville, AR 72701, USA
[17] Indian Institute of Astrophysics, Block II, Koramangala, Bangalore 560034, India
[18] MPE, Giessenbachstrasse 1, Garching D-85748, Germany
[19] INAF, Osservatorio Astrofisico di Firenze, Largo Enrico Fermi 5, I-50125, Firenze, Italy
[20] Leibniz-Institut fuer Astrophysik Potsdam (AIP), An der Sternwarte 16, D-14482 Potsdam, Germany
[21] Inter-university Institute for Data Intensive Astronomy, Department of Physics and Astronomy, University of the Western Cape, Robert Sobukwe Road, 7535, Bellville, Cape Town, South Africa
[22] INAF—Istituto di Radioastronomia, via Gobetti 101, I-40129 Bologna, Italy
[23] Dipartimento di Fisica e Astronomia, Università degli Studi di Bologna, via Gobetti 93/2, I-40129 Bologna, Italy
[24] INAF—Osservatorio di Astrofisica e Scienza dello Spazio di Bologna—via Gobetti 93/3, I-40129 Bologna, Italy
[25] Scuola Normale Superiore, Piazza dei Cavalieri 7, I-56126, Pisa, Italy
[26] CAS Key Laboratory for Research in Galaxies and Cosmology, Department of Astronomy, University of Science and Technology of China, Hefei 230026, People's Republic of China
[27] School of Astronomy and Space Sciences, University of Science and Technology of China, Hefei 230026, People's Republic of China
[28] School of Physics & Astronomy, University of Southampton, Highfield Campus, Southampton S017 1BJ, UK
[29] CSIRO Astronomy and Space Science, P.O. Box 76, Epping, NSW, 1710, Australia
[30] German Aerospace Center (DLR), Space Operation and Astronaut Training, Oberpfaffenhofen, D-82234 Weßling, Germany
[31] Department of Physics and Astronomy, The University of Sheffield, Hounsfield Road, Sheffield, S3 7RH, UK
[32] Dipartimento di Fisica, Universitàdi Napoli "Federico II," via Cinthia 9, I-80126 Napoli, Italy
[33] INAF—Osservatorio Astronomico di Capodimonte, Salita Moiariello 16, I-80131, Napoli, Italy
[34] INFN—Sezione di Napoli, via Cinthia 9, I-80126 Napoli, Italy
[35] Department of Physics, University of North Texas, Denton, TX 76203, USA
[36] Department of Astronomy, Xiamen University, Xiamen, Fujian 361005, People's Republic of China
[37] Department of Physics, University of Connecticut, 2152 Hillside Road, Unit 3046, Storrs, CT 06269, USA
Received 2021 April 5; revised 2021 June 3; accepted 2021 June 17; published 2021 September 14

Abstract

We present the X-ray point-source catalogs in two of the XMM-Spitzer Extragalactic Representative Volume Survey (XMM-SERVS) fields, W-CDF-S (4.6 $\deg^2$) and ELAIS-S1 (3.2 $\deg^2$), aiming to fill the gap between deep pencil-beam X-ray surveys and shallow X-ray surveys over large areas. The W-CDF-S and ELAIS-S1 regions were targeted with 2.3 and 1.0 Ms of XMM-Newton observations, respectively; 1.8 and 0.9 Ms exposures remain after flare filtering. The survey in W-CDF-S has a flux limit of 1.0×10^{-14} erg cm^{-2} s^{-1} over 90% of its area in the 0.5–10 keV band; 4053 sources are detected in total. The survey in ELAIS-S1 has a flux limit of 1.3×10^{-14} erg cm^{-2} s^{-1} over 90% of its area in the 0.5–10 keV band; 2630 sources are detected in total. Reliable optical-to-IR multiwavelength counterpart candidates are identified for ≈89% of the sources in W-CDF-S and ≈87% of the sources in ELAIS-S1. A total of 3129 sources in W-CDF-S and 1957 sources in ELAIS-S1 are classified as active galactic nuclei (AGNs). We also provide photometric redshifts for X-ray sources; ≈84% of the 3319/2001 sources in W-CDF-S/ELAIS-S1 with optical-to-near-IR forced photometry available have either spectroscopic redshifts or high-quality photometric redshifts. The completion of the XMM-Newton observations in the W-CDF-S and ELAIS-S1 fields marks the end of the XMM-SERVS survey data gathering. The ≈12,000 pointlike X-ray sources detected in the whole ≈13 $\deg^2$ XMM-SERVS survey will benefit future large-sample AGN studies.

Unified Astronomy Thesaurus concepts: Catalogs (205); Surveys (1671); Active galactic nuclei (16); Active galaxies (17); X-ray active galactic nuclei (2035); X-ray point sources (1270); X-ray quasars (1821); X-ray surveys (1824)

Supporting material: machine-readable tables

1. Introduction

Owing to the penetrating nature of X-rays and their reduced dilution by host-galaxy starlight, X-ray surveys have been effectively utilized to identify reliable and nearly complete samples of active galactic nuclei (AGNs), which provide essential insights into the demographics, ecology, and physics of growing supermassive black holes (SMBHs) over most of cosmic history (e.g., Brandt & Alexander 2015; Xue 2017).

XMM-Newton and Chandra surveys have provided the most efficient method in assembling reliable and quite complete samples of distant AGNs, including obscured systems otherwise difficult to find. The currently publicly available wide-field X-ray surveys such as the 8–10 ks depth XMM-Newton Stripe 82X (LaMassa et al. 2016) and XMM-XXL (e.g., Liu et al. 2016) have made excellent progress sampling the luminous AGN populations and their environments. At the same time, they lack the sensitivity to detect the bulk of SMBH growth, as they only probe ≈2–6 times below the knee of the X-ray luminosity function at $z = 0.5$–2.5, and the AGNs detected produce less than half of cosmic accretion power (e.g., Ueda et al. 2014; Aird et al. 2015). The narrow-field deep X-ray surveys (0.11.1 deg^2), such as the CDF-S (Luo et al. 2017), CDF-N (Xue et al. 2016), E-CDF-S (Xue et al. 2016), AEGIS-X (Nandra et al. 2015), and SXDS (Ueda et al. 2008), are able to sample AGNs that produce the bulk (>70%) of cosmic accretion power at $z \lesssim 3$–5 well (e.g., Ueda et al. 2014; Aird et al. 2015; Vito et al. 2018). However, they do not have the contiguous volume needed to explore AGN activity over a wide dynamic range of cosmic environments and to sample substantially the high-luminosity tail of the AGN population. Simulations indicate that at $z \approx 1$ the largest structures (e.g., superclusters) extend up to 2–3 deg^2 on the sky (e.g., Klypin et al. 2016). Thus, even the ≈2 deg^2 COSMOS field (e.g., Cappelluti et al. 2009; Civano et al. 2016) is not able to sample the full range of cosmic environments. Therefore, it is necessary to obtain several distinct medium-deep X-ray surveys, each over several deg^2, in addition to COSMOS for investigating SMBH growth across the full range of cosmic environments and minimizing cosmic variance (e.g., Driver & Robotham 2010; Moster et al. 2011).

To this end, we designed an XMM-Newton survey, XMM-SERVS, to provide medium-deep X-ray coverage in the SERVS (Mauduit et al. 2012) regions of the W-CDF-S (≈4.6 deg^2), ELAIS-S1 (≈3.2 deg^2), and XMM-LSS (≈5.3 deg^2) fields, all of which have superb multiwavelength coverage. The point-source catalog for the XMM-LSS field has been published in Chen et al. (2018). In this work, we provide point-source catalogs for the two remaining fields, W-CDF-S and ELAIS-S1. Data products from the full XMM-SERVS survey (including all the three fields) are available online.[38]

The paper is structured as follows. Section 2 describes the new XMM-Newton observations in the W-CDF-S and ELAIS-S1 fields, as well as overlapping archival multiwavelength data in these areas. Section 3 presents the X-ray source detection process and the properties of the derived X-ray sources. Section 4 describes the multiwavelength counterpart identification process for the X-ray sources. Section 5 presents spectroscopic redshifts and photometric redshifts of X-ray sources. In Section 6, basic AGN classification is presented. Section 7 gives the summary of the work. Appendix A describes the columns included in our X-ray source catalogs. Appendix B describes the identification of broad-line (BL) AGNs among the X-ray sources detected. Appendix C describes the classification of X-ray sources that are not AGNs. A ΛCDM cosmology with $H_0 = 70\,\mathrm{km\,s^{-1}\,Mpc^{-1}}$, $\Omega_m = 0.3$, and $\Omega_\Lambda = 0.7$ is assumed throughout the paper. A Galactic column density $N_\mathrm{H} = 8.4 \times 10^{19}\,\mathrm{cm^{-2}}$ is adopted for the W-CDF-S field, and $N_\mathrm{H} = 3.4 \times 10^{20}\,\mathrm{cm^{-2}}$ is adopted for the ELAIS-S1 field (Willingale et al. 2013).

2. XMM-Newton Observations in the W-CDF-S and ELAIS-S1 Regions

2.1. Multiwavelength Data Coverage and Archival XMM-Newton and Chandra Observations in the W-CDF-S Region

There are deep archival Chandra and XMM-Newton observations in the center of the ≈4.5 deg^2 W-CDF-S field, covering a relatively small area (see Figure 1). The Chandra Deep Field-South (CDF-S) survey has now reached a 7 Ms depth, covering 482 $'^2$ (e.g., Xue et al. 2011; Luo et al. 2017); XMM-Newton has also observed this field for 3.3 Ms (covering ≈790 $'^2$; e.g., Comastri et al. 2011; Ranalli et al. 2013). The 250 ks Extended Chandra Deep Field-South (E-CDF-S) survey further increases the X-ray coverage to 1128.′6 ^{2} (e.g., Xue et al. 2016). There are also several additional ≈5–15 ks Chandra observations in the W-CDF-S region (including four observations just to the south of E-CDF-S; PI: W. N. Brandt). These Chandra data are utilized in our study to help the multiwavelength counterpart matching of XMM-Newton sources (see Section 4). All of the above X-ray observations, along with the multiwavelength data, have enabled many AGN studies.

The W-CDF-S region, which is ≈ 30 times larger in solid angle than the original CDF-S, also has extensive multiwavelength coverage (see Table 1 for a list of the key multiwavelength photometric data). It aligns with one of the well-studied Spitzer Extragalactic Representative Volume Survey (SERVS; Mauduit et al. 2012) fields, and it is also one of the deep drilling fields of the upcoming Legacy Survey of Space and Time (LSST) to be conducted by the Vera C. Rubin Observatory (e.g., Brandt et al. 2018; Scolnic et al. 2018). With the XMM-SERVS survey covering the W-CDF-S region, multiwavelength data in this area can be utilized together with the X-ray data, enabling large-sample studies of AGNs and other X-ray sources.

2.2. Multiwavelength Data Coverage and Archival XMM-Newton and Chandra Observations in the ELAIS-S1 Region

About 0.6 deg^2 of the ≈3 deg^2 ELAIS-S1 region has been targeted with both XMM-Newton (≈50 ks depth) and Chandra (≈ 30 ks depth) (e.g., Puccetti et al. 2006; Feruglio et al. 2008). There are also several additional Chandra observations in the ELAIS-S1 region. The multiwavelength data coverage of the

[38] https://personal.psu.edu/wnb3/xmmservs/xmmservs.html

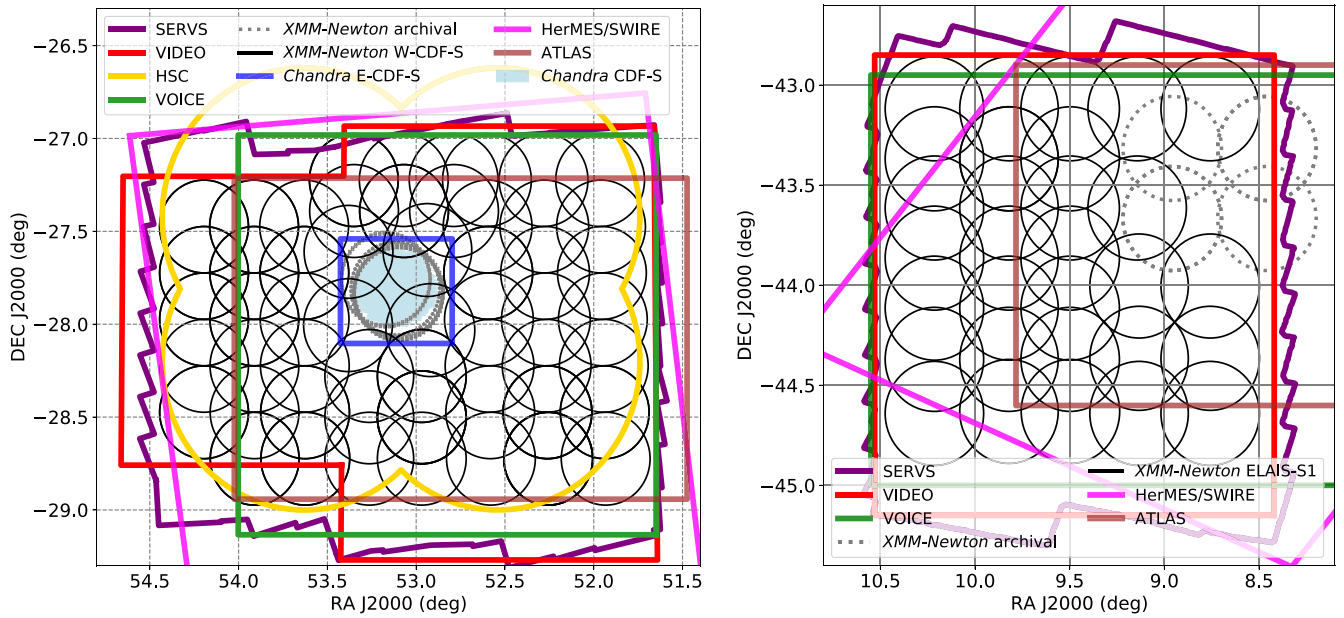

Figure 1. Left: locations of the XMM-Newton observations in the W-CDF-S field (black circles), presented together with the multiwavelength coverage from selected surveys and the primary archival X-ray observations in this area (as labeled in the figure key). The DES wide-field survey (see Table 1) in the optical covers the whole area and thus is not plotted in the figure. Right: locations of the XMM-Newton observations in the ELAIS-S1 field (black circles), presented together with the selected multiwavelength coverage and the primary archival X-ray observations in this area (as labeled in the figure key). The DES wide-field survey and ESIS (see Table 1) in the optical cover the whole area and thus are not plotted in the figure.

Table 1
Key Multiwavelength Imaging Coverage of the W-CDF-S and ELAIS-S1 Fields

Band	Field(s)[a]	Survey Name	Coverage; Notes	Example Reference
Radio	C/E	Australia Telescope Large Area Survey (ATLAS)	3.6/2.7 deg^2; 14/17 μJy rms depth at 1.4 GHz	Franzen et al. (2015)
	C/E	MIGHTEE Survey (in progress)	3/4.5 deg^2; 1 μJy rms depth at 1.4 GHz	Jarvis et al. (2016)
MIR–FIR	C/E	Herschel Multi-tiered Extragal. Surv. (HerMES)	11.4/3.7 deg^2; 5–60 mJy depth at 100–500 μm	Oliver et al. (2012)
	C/E	Spitzer Wide-area IR Extragal. Survey (SWIRE)	7.1/14.3 deg^2; 0.01–200 mJy depth at 3.6–160 μm	Vaccari (2015)
NIR	C/E	Spitzer survey of Deep Drilling Fields (DeepDrill)	9/9 deg^2; 2 μJy depth at 3.6 and 4.5 μm	Lacy et al. (2021)
	C/E	Spitzer Extragal. Rep. Vol. Survey (SERVS)	4.5/3 deg^2; 2 μJy depth at 3.6 and 4.5 μm	Mauduit et al. (2012)
	C/E	VISTA Deep Extragal. Obs. Survey (VIDEO)	4.5/3 deg^2; $ZYJHK_s$ to $m_{AB} \approx 23.8$–25.7	Jarvis et al. (2013)
Optical	C/E	Dark Energy Survey (DES) Data Release 2	9/6 deg^2; *grizy* to $m_{AB} \approx 23$–25.5	Abbott et al. (2021)
	C	Hyper Suprime Cam (HSC) optical imaging	5.7 deg^2; *griz* to $m_{AB} \approx 25$–26	Ni et al. (2019)
	C	VST Opt. Imaging of CDF-S and ES1 (VOICE)	4 deg^2; *ugri* to $m_{AB} \approx 26$	Vaccari et al. (2016)
	E	VST Opt. Imaging of CDF-S and ES1 (VOICE)	4 deg^2; *u* to $m_{AB} \approx 26$, *gri* observations planned	Vaccari et al. (2016)
	C	SWIRE optical imaging	7.1 deg^2; $u'g'r'i'z'$ to $m_{AB} \approx 23$–25	Lonsdale et al. (2003)
	E	ESO-Spitzer Imaging Extragalactic Survey (ESIS)	4.5 deg^2; *BVR* to $m_{AB} \approx 24$–25	Berta et al. (2006)
	C/E	LSST deep drilling field (Planned)	10/10 deg^2; *ugrizy* to $m_{AB} \approx 26$–28	Brandt et al. (2018)
UV	C/E	GALEX Deep Imaging Survey	7/15 deg^2; NUV, FUV to $m_{AB} \approx 24$–24.5	Martin et al. (2005)

Note.
[a] "C" stands for W-CDF-S; "E" stands for ELAIS-S1.

ELAIS-S1 field is listed in Table 1. Similar to the W-CDF-S field, ELAIS-S1 aligns with one of the SERVS fields and will be one of the LSST deep drilling fields. As can be seen in Table 1, the optical data in ELAIS-S1 are not yet as deep as those in W-CDF-S (see also Zou et al. 2021 for further details).

2.3. New XMM-Newton Observations and Data Reduction

XMM-Newton observations in the W-CDF-S field were obtained between 2018 July and 2021 January (see the left panel of Figure 1 for the pointing layout) with a total of 2.3 Ms exposure time, including 80 successful observations. For the ELAIS-S1 field, XMM-Newton observations were performed between 2019 May and 2020 December (see the right panel of Figure 1 for the pointing layout), with a total of 1.0 Ms exposure time, including 31 successful observations. All the observations were performed with a THIN filter for the EPIC cameras, and Optical Monitor data were taken in parallel as well (we do not include these data in our catalogs, due to the existing optical/UV coverage listed in Table 1). As these fields are far from the Galactic plane, the numbers of very bright stars in these fields are small, and the optical loading effects for the X-ray CCDs are negligible. The details of each observation are

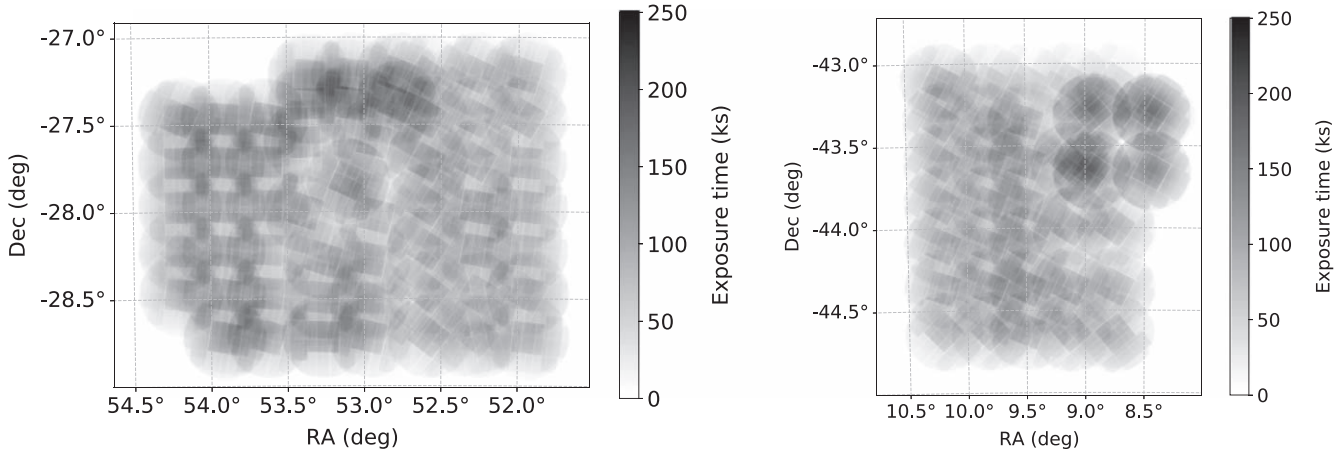

Figure 2. Left: effective exposure map (PN + MOS) in the full band for W-CDF-S. The XMM-Newton coverage in the survey region is generally uniform. Right: similar to the left panel, but for ELAIS-S1.

Table 2
XMM-Newton Observations in the W-CDF-S and ELAIS-S1 Fields

Field	Revolution	ObsID	UT Date	R.A. (deg)	Decl. (deg)	GTI (PN) (ks)	GTI (MOS1) (ks)	GTI (MOS2) (ks)	Expo (ks)
W-CDF-S	3403	0827210101	2018-07-08 23:34:26	52.579042	−28.723972	27.9	30.5	29.7	33
W-CDF-S	3403	0827210201	2018-07-09 09:04:26	52.582875	−28.473972	27.9	29.4	29.2	33
W-CDF-S	3406	0827210301	2018-07-15 05:20:04	52.586667	−28.223972	28.9	30.7	30.6	33
ELAIS-S1	3561	0827251301	2019-05-20 07:26:00	9.143708	−43.614139	28.8	30.5	30.6	33
ELAIS-S1	3568	0827240101	2019-06-03 05:48:52	8.757958	−44.004000	29.4	31.6	31.3	34

Note. Columns from left to right: target field; XMM-Newton revolution; XMM-Newton Observation ID; observation starting date/time; R.A. and decl. of the pointing center (J2000, degrees); cleaned exposure time (included in the "good time intervals"; GTIs) for PN, MOS1, and MOS2 in each pointing; total EPIC exposure time (during which PN, MOS1, and MOS2 take exposures simultaneously).

(This table is available in its entirety in machine-readable form.)

listed in Table 2. As described in Chen et al. (2018), we first observed the desired pointings with 33 ks exposures and then reobserved the sky regions strongly affected by XMM-Newton background flaring to achieve better uniformity. For the W-CDF-S field, we do not reanalyze all of the archival XMM-Newton observations of the CDF-S proper (which cover $\approx$0.25 deg^2) in this work; instead, we selected one observation (ObsID: 0604960501) from the archival data to reach a uniform depth across the W-CDF-S field and process this consistently in the same manner as the rest of our data. For the ELAIS-S1 field, all the archival XMM-Newton observations are included in the analyses.

The XMM-Newton Science Analysis System (SAS) 19.0.0[39] and HEASOFT 6.26[40] are utilized for our data analysis. We use the SAS tasks `epproc` and `emproc` to process the XMM-Newton Observation Data Files (ODFs), creating MOS1, MOS2, PN, and PN out-of-time (OOT) event files for each observation ID. Following Section 2.2 of Chen et al. (2018), single-event light curves are created for each event file in time bins of 100 s at high (10–12 keV) and low (0.3–10 keV) energies to select time intervals without significant background flares (the "good time intervals"; GTIs); we note that real sources provide minimal contributions to these total event file light curves. For the 10–12 keV light curve, we remove time intervals with count rates $>3\sigma$ above the mean count rate. The same procedure is also performed for the 0.3–10 keV light curves. For a small number of event files with intense background flares, the event files are filtered using the nominal count-rate thresholds suggested by the XMM-Newton Science Operations Centre.[41]

For the W-CDF-S field, a total of 1.8 Ms (1.5 Ms) of MOS (PN) exposure remains after flare filtering; for the ELAIS-S1 field, a total of 0.9 Ms (0.8 Ms) of MOS (PN) exposure remains. We do not exclude events in energy ranges that overlap with the instrumental background lines (Al Kα lines at 1.39–1.55 keV for MOS and PN; Cu lines at 7.35–7.60 keV and 7.84–8.28 keV for PN; Si lines at 1.691.80 keV for MOS), as keeping these events improves the positional accuracy of the detected sources owing to the higher number of counts detected.

We use `evselect` to construct images with a 4″ pixel size from the flare-filtered event file in the full band (0.2–12 keV). We use `eexpmap` to generate exposure maps with USEFASTPIXELIZATION = 0 and ATTREBIN = 0.5, both with and without vignetting corrections. Detector masks were constructed with `emask`. The mosaicked vignetting-corrected PN+MOS1+MOS2 exposure map in the W-CDF-S/ELAIS-S1 field and the distribution of the exposure time across the survey field are presented in Figures 2 and 3. As can be seen in Figure 3, $\approx$4.6 deg^2 of the W-CDF-S field is covered by XMM-Newton; $\approx$3.2 deg^2 of the ELAIS-S1 field is covered

[39] https://www.cosmos.esa.int/web/xmm-newton/sas-release-notes-1900
[40] https://heasarc.gsfc.nasa.gov/FTP/software/ftools/release/archive/Release_Notes_6.26
[41] https://www.cosmos.esa.int/web/xmm-newton/sas-thread-epic-filterbackground

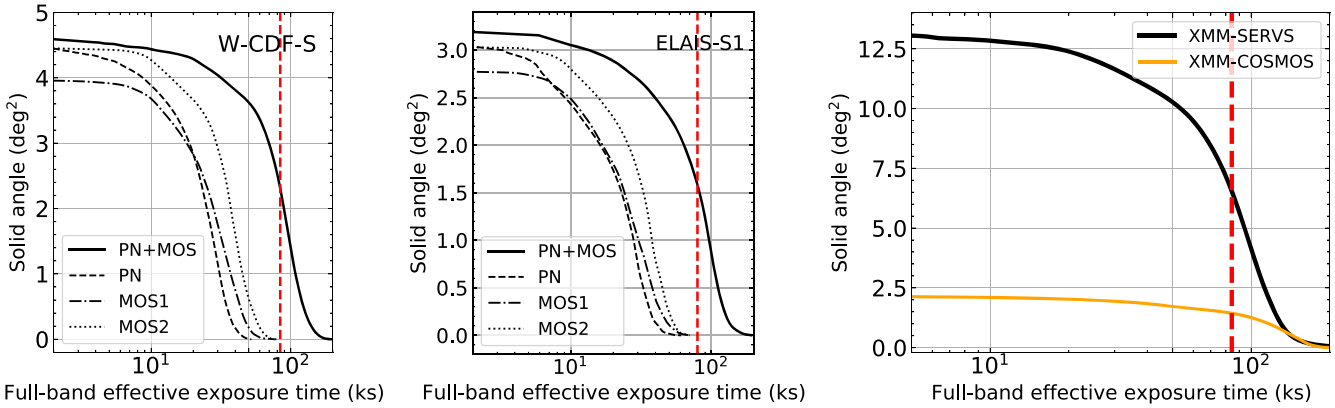

Figure 3. Cumulative survey solid angle as a function of full-band effective (i.e., vignetted) exposure in W-CDF-S (left), ELAIS-S1 (middle), and the entire XMM-SERVS survey (right). The black solid/dashed/dashed–dotted/dotted line is for the PN+MOS/PN/MOS1/MOS2 exposure. The relatively small solid angle of MOS1 coverage is due to the lost CCDs for MOS1. The solid orange line in the right panel is for the PN+MOS exposure in XMM-COSMOS (Cappelluti et al. 2009). The red vertical line marks the median exposure.

by XMM-Newton. The median PN+MOS1+MOS2 exposure time across the W-CDF-S/ELAIS-S1 field is ≈84/80 ks. More than 80% of the W-CDF-S/ELAIS-S1 footprints have PN+MOS1+MOS2 exposure time ≳47/37 ks. Figure 3 shows the cumulative survey solid angle as a function of full-band effective exposure for the full three-field XMM-SERVS survey. The median PN+MOS1+MOS2 exposure time across the full XMM-SERVS survey field is ≈85 ks.

3. Source Detection and the Main X-Ray Source Catalogs

3.1. First-pass Source Detection and Astrometric Correction

Following Chen et al. (2018), we run a first-pass source detection in the full band to register the XMM-Newton observations onto a common World Coordinate System (WCS) frame with the following steps:

1. For each observation, `eboxdetect` is used to generate a temporary source list with LIKEMIN = 8 for each of the three instruments.
2. This temporary source list is utilized to generate background images for each instrument (with the input sources removed), using `esplinemap` with METHOD = ASMOOTH. This adaptive-smoothing method has been widely adopted in recent XMM-Newton catalogs (e.g., Traulsen et al. 2019, 2020; Webb et al. 2020), as it can well characterize the local X-ray background level.
3. We run `eboxdetect` again in the map mode (with LIKEMIN = 8), combining images, exposure maps, and background maps from all the instruments for each observation.
4. With this new source list generated by `eboxdetect` as the input, the PSF fitting tool `emldetect` is used to determine the X-ray positions and detection likelihoods utilizing all the instruments of each observation. We only keep the pointlike sources, and a stringent likelihood threshold (LIKEMIN = 10.8) is adopted to ensure that astrometric corrections are calculated based on significant detections that are unlikely to be spurious.

For each observation, we use CATCORR to match the output source list from `emldetect` with an optical/IR reference catalog (available from the relevant XMM-Newton Processing Pipeline Subsystem products; Rosen et al. 2016) created from the Sloan Digital Sky Survey (SDSS; Abazajian et al. 2009), Two Micron All Sky Survey (Skrutskie et al. 2006), and USNO-B1.0 (Monet et al. 2003) catalogs. By matching the X-ray sources to the reference catalogs (the median number of matched sources is 18 among all the observations), the needed astrometric offsets and rotation corrections are calculated. The R.A./decl. offsets are typically $\lesssim 3''$. The rotation corrections are less than ≈0.17 deg. The event files and the attitude file for each observation are then projected onto the new frame.

3.2. Second-pass Source Detection

Using the astrometry-corrected event files, we recreate images (see Figure 4 for the smoothed full-field mosaicked XMM-Newton images for W-CDF-S and ELAIS-S1, and Figure 5 for an example cutout of the smoothed mosaicked image in W-CDF-S), exposure maps, detector masks, and background maps in five bands: band 1 (0.2–0.5 keV), band 2 (0.5–1.0 keV), band 3 (1.0–2.0 keV), band 4 (2.0–4.5 keV), and band 5 (4.5–12 keV). We define the full band as bands 1–5 (0.2–12 keV), soft band as bands 1–3 (0.2–2 keV), and hard band as bands 4–5 (2–12 keV). Exposure maps and image mosaics are also created for the full/soft/hard band combining all the observations and instruments in the full/soft/hard band. We then run source detection again with data products from bands 1, 2, 3, 4, and 5, combining all XMM-Newton observations together. This five-band detection approach has been widely adopted in XMM-Newton catalogs (e.g., Rosen et al. 2016; Traulsen et al. 2019, 2020; Webb et al. 2020) since it improves the positional accuracy of sources detected compared to single-band detections. When detecting sources in the full band (0.2–12 keV), we use bands 1–5 simultaneously; when detecting sources in the soft band (0.2–2 keV), we use bands 1–3 simultaneously; when detecting sources in the hard band (2–12 keV), we use bands 4–5 simultaneously. As `emldetect` can only process a limited number of observations, we divide the W-CDF-S/ELAIS-S1 field into a grid when performing the second-pass source detection (e.g., Chen et al. 2018). For each cell in the grid, we co-add the images and exposure maps for all observations inside the cell and run `ewavelet` with a low detection threshold (4) in the full/soft/hard band. The source list obtained from `ewavelet` is then utilized as the input for `emldetect` (only sources within the celestial coordinate range of the cell plus 1′ "padding" on each side of the cell are kept). The full/soft/hard-band source list from `emldetect` in each cell is then combined to remove duplications

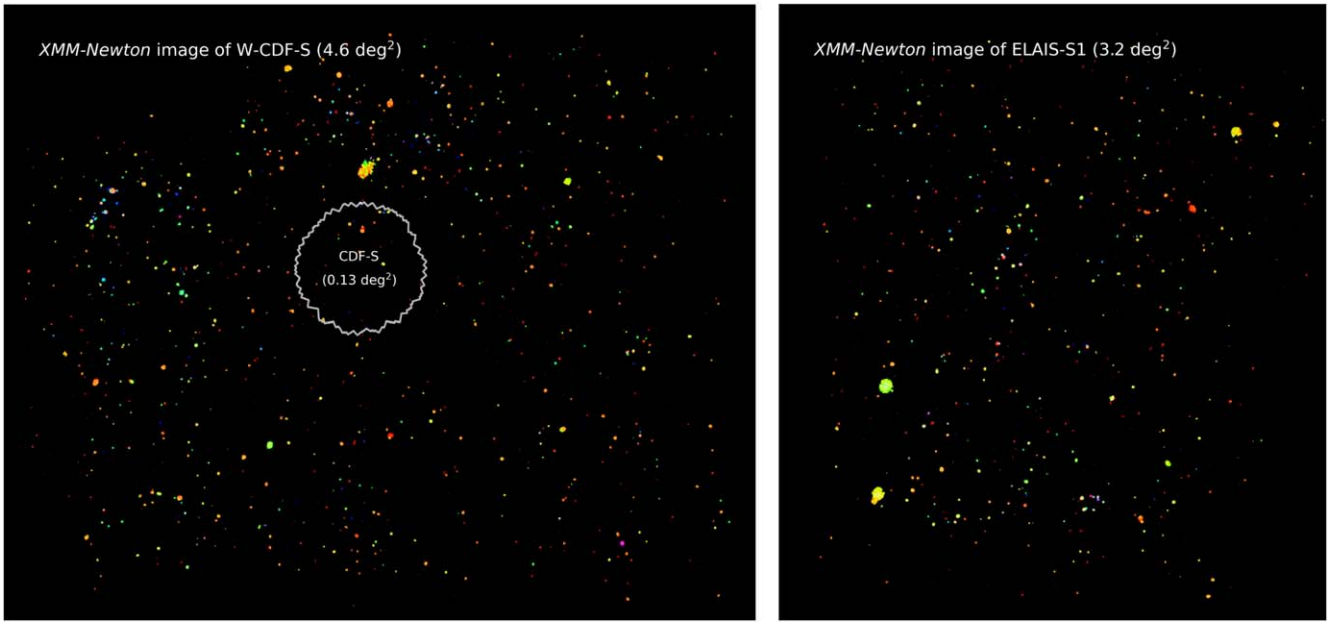

Figure 4. Left: "false-color" smoothed X-ray image of W-CDF-S. Band 1+2, band 3, and band 4+5 are represented by the colors red, green, and blue, respectively. Redder sources are softer; bluer sources are harder. An asinh stretch is utilized. The white solid curve indicates the footprint of the 7 Ms CDF-S (Luo et al. 2017). Right: similar to the left panel, but for the ELAIS-S1 field.

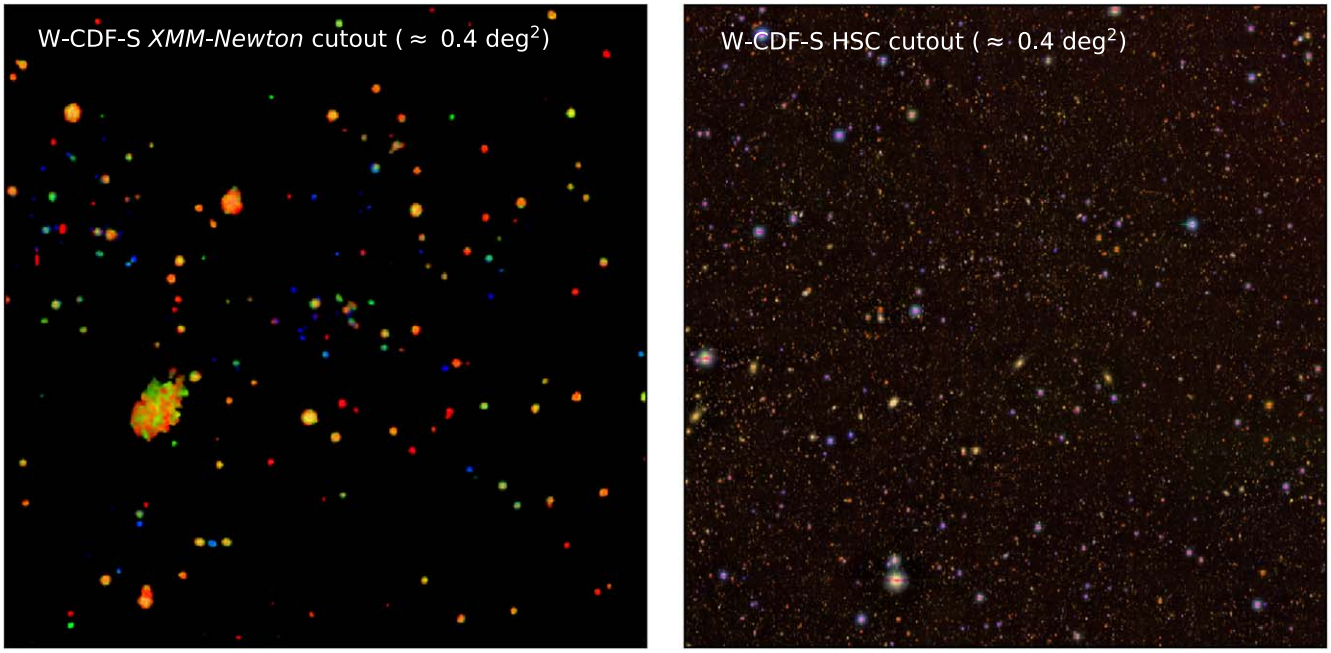

Figure 5. Left: example "false-color" smoothed X-ray image cutout of W-CDF-S with field size ≈0.4 deg^2 and central R.A. = 52.°9 and decl. = −27.°4. Band 1+2, band 3, and band 4+5 are represented by the colors red, green, and blue, respectively. Redder sources are softer; bluer sources are harder. An asinh stretch is utilized. The large extended source toward the lower left is an X-ray cluster at $z = 0.15$. Right: example "false-color" optical image of W-CDF-S in the same sky area as that of the left panel. The $g/i/z$-band HSC image is represented by the color blue/green/red.

(sources in the "padding" area that do not have duplications within 10″ are kept). For each band in each field, we select sources with detection likelihoods (DET_ML) larger than the threshold that corresponds to a 1% spurious fraction according to simulations (see Section 3.3 for details).

3.3. Simulations to Assess Catalog Reliability

Similar to Chen et al. (2018), we perform Monte Carlo simulations of the X-ray observations in W-CDF-S and ELAIS-S1 to assess the reliability of the source catalogs. For each simulation, we generate mock X-ray sources using the Kim et al. (2007) log N-log S relations. The minimum simulated flux is set to be 0.5 dex lower than the minimum detected flux; the maximum flux is set to be 10^{-11} erg cm^{-2} s^{-1}. We then use CDFS-SIM[42] to convert fluxes to PN/MOS count rates, and place sources at random sky positions, thus creating mock event files. The

[42] https://github.com/piero-ranalli/cdfs-sim

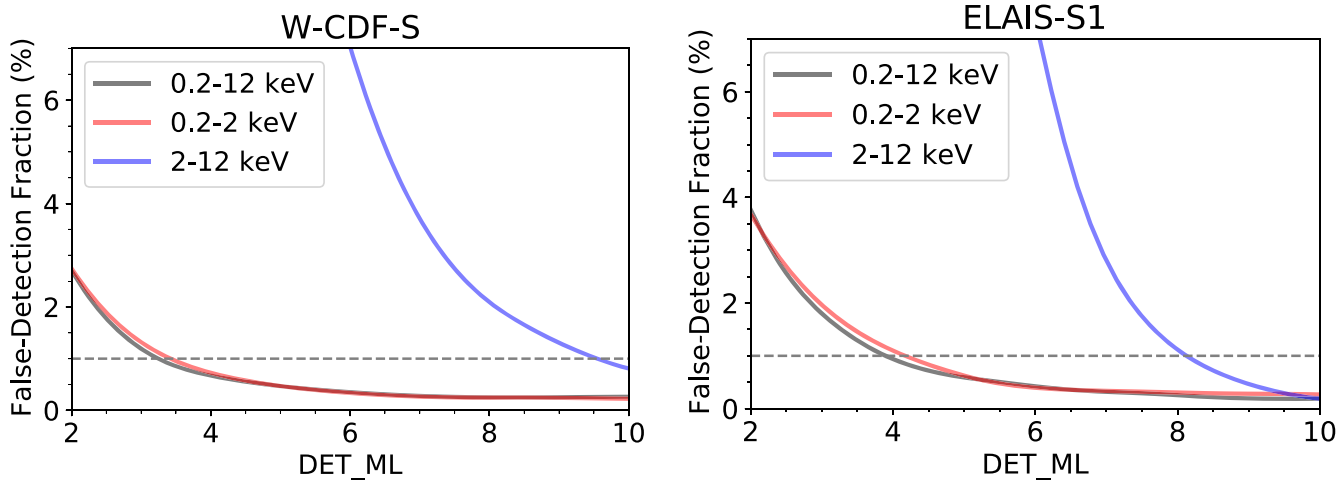

Figure 6. Left: the fraction of spurious sources as a function of DET_ML threshold based on simulations. The horizontal dashed line marks a spurious fraction of 1%, which determines the DET_ML thresholds adopted for W-CDF-S. Right: similar to the left panel, but for the ELAIS-S1 field.

images are extracted in the same manner as the real ones. The background is simulated by re-sampling the original background map according to a Poisson distribution. A total of 10 simulations are created for each energy band. The same two-stage source detection procedures are performed on the simulated data; the detected sources are matched to input sources within a 10″ cut-off radius by minimizing the quantity R^2:

$$R^2 = \left(\frac{\Delta \mathrm{R.A.}}{\sigma_{\mathrm{R.A.}}}\right)^2 + \left(\frac{\Delta \mathrm{Decl.}}{\sigma_{\mathrm{decl.}}}\right)^2 + \left(\frac{\Delta \mathrm{RATE}}{\sigma_{\mathrm{RATE}}}\right)^2, \quad (1)$$

where ΔR.A. /ΔDecl. /ΔRATE is the difference between the R.A./decl./count rate of matched detected sources and input sources; $\sigma_{\mathrm{R.A.}}/\sigma_{\mathrm{decl.}}/\sigma_{\mathrm{RATE}}$ is the uncertainty of the detected sources in R.A./decl./count rate. Detected sources without any input sources within 10″ are considered to be spurious detections.

The left/right panel of Figure 6 presents the average spurious fraction (f_{spurious}) as a function of DET_ML in the full/soft/hard band for the W-CDF-S/ELAIS-S1 field obtained from the simulations we ran. To achieve $f_{\mathrm{spurious}} \lesssim 1\%$ for the W-CDF-S field, a DET_ML threshold of ≈3.5/3.5/9.5 is needed for the full/soft/hard band. For the ELAIS-S1 field, a DET_ML threshold of ≈4.0/4.0/8.0 is required for the full/soft/hard band. In the soft band, the background levels are similar for the W-CDF-S and ELAIS-S1 fields. Thus, due to the slightly larger amount of exposure time in W-CDF-S than ELAIS-S1, the DET_ML threshold in the soft band for the W-CDF-S field is slightly smaller than that for the ELAIS-S1 field. In the hard band, the background level for the W-CDF-S field is higher compared to the ELAIS-S1 field. Thus, the DET_ML threshold in the hard band for the W-CDF-S field is larger than that for the ELAIS-S1 field. The source signal in the full band is typically dominated by the source signal from the soft band, so that the DET_ML threshold in the full band is close to that in the soft band.

3.4. Astrometric Accuracy

To estimate the positional accuracy of the detected XMM-Newton sources in the full/soft/hard band, we first matched the sources with optical catalogs. As described in Chen et al. (2018), directly matching X-ray sources to optical counterparts can be associated with a relatively high false-match rate (≈18%). We therefore chose NWAY (Salvato et al. 2018; see Section 4 for a basic description ofNWAY) to match XMM-Newton sources with optical/near-IR (NIR) counterparts with priors as described in Section 4 within 10″, using an iterative method. In the NIR, we use Spitzer data from the DeepDrill data release (Lacy et al. 2021) that includes the SERVS data (Mauduit et al. 2012), and VISTA data from the VIDEO data release in 2020 (M. Jarvis et al. 2021, private communication) for both the W-CDF-S and ELAIS-S1 fields. In the optical, we use HSC data from Ni et al. (2019) for W-CDF-S and DES DR2 data (Abbott et al. 2021) for ELAIS-S1 (see Table 1 for the survey descriptions). Since a small fraction of X-ray sources in the W-CDF-S field lack HSC coverage (see Figure 1), we add DES DR2 sources (Abbott et al. 2021) in the W-CDF-S field that have no HSC counterpart within 1″ to the HSC catalog;this also provides optical coverage in the saturated regions of the HSC image. In the first iteration, we adopt the quadrature combination of the positional uncertainty derived from emldetect (σ_{eml}) and a constant 0.″5 systematic uncertainty as the positional uncertainty of XMM-Newton sources (σ_x). The positional uncertainties adopted for optical/NIR sources are listed in Table 4. We then select all the X-ray sources in W-CDF-S/ELAIS-S1 with HSC/DES counterparts that have $p_{\mathrm{any}} > 0.1$ (which is the threshold adopted in this work, corresponding to a false-match rate of ∼5%; see Section 4.3 and Figure 19).[43] We also exclude ≈4% X-ray sources and their matched optical counterparts that have positional offsets greater than $3\sigma_x$ from the analysis. We fit the separations between X-ray sources and optical sources as a linear function of source counts (C) in W-CDF-S and ELAIS-S1, respectively,[44] and then adjust the intercept so that 68% of the sources have positional offsets smaller than the expectation from the relation (see Figure 7 for the obtained relations in the full band). The intercept and slope are taken as the parameters for the empirical relation between

[43] p_{any} is a parameter in the NWAY output, representing the probability for the source to have any counterpart.

[44] The X-ray positional uncertainty is typically associated with both C and the off-axis angle (see Luo et al. 2017; Chen et al. 2018 for details). For the XMM-SERVS survey, most of the sources are detected in multiple observations, so that their effective average off-axis angles do not vary significantly. Thus, we only associate σ_x with C in this work.

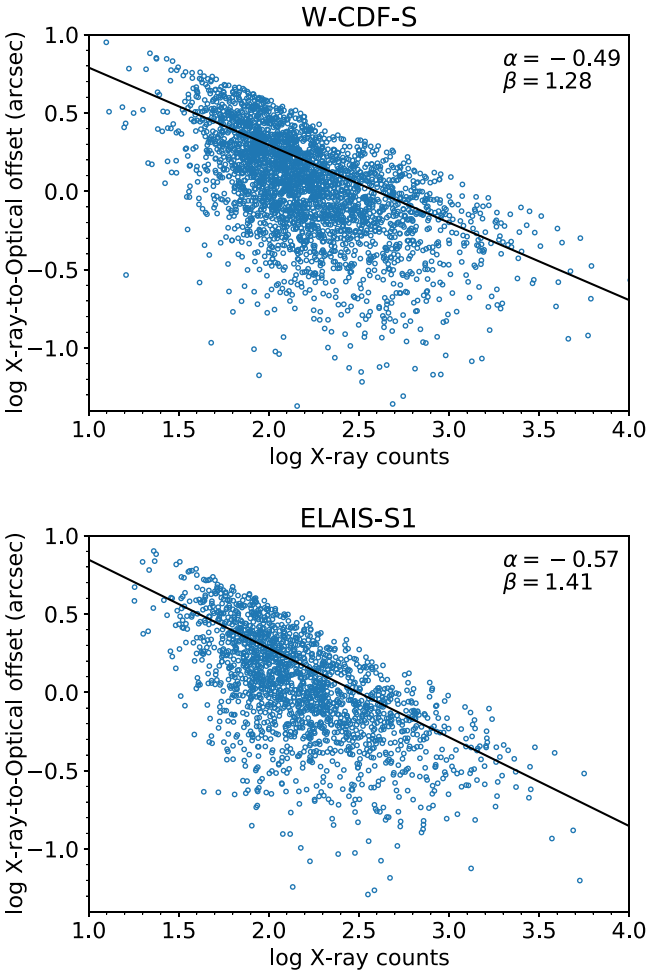

Figure 7. The positional offsets between detected X-ray sources in the full band and their matched optical counterparts vs. the full-band X-ray source counts number (C) in W-CDF-S (top) and ELAIS-S1 (bottom). The derived relation between $\log_{10} r_{68\%}$ and C is marked as the black solid line.

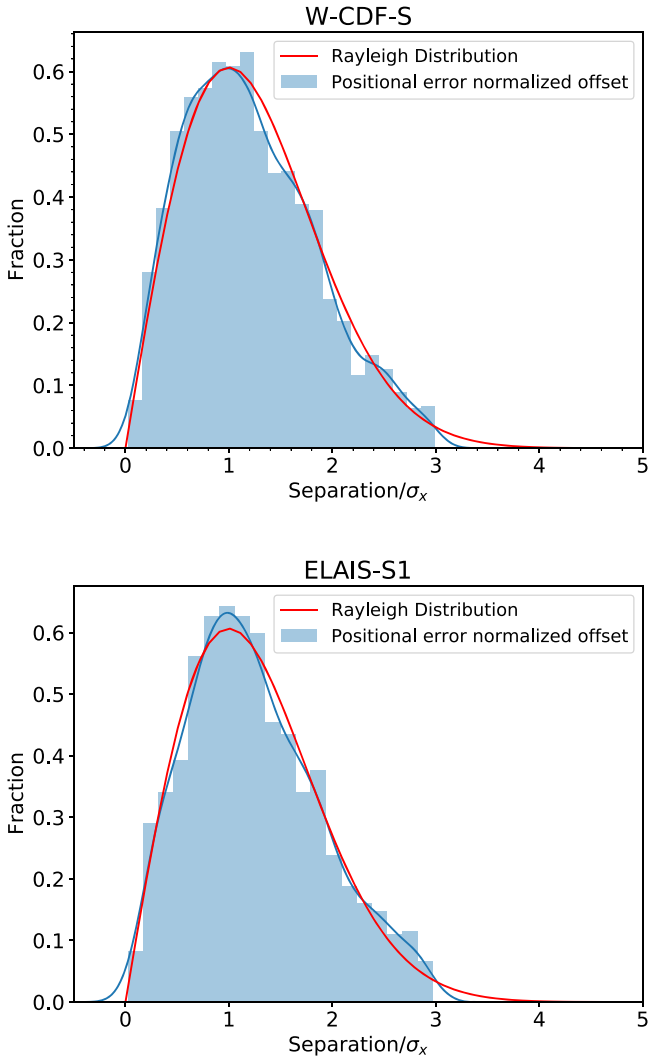

Figure 8. Comparison between the distribution of the separations between the full-band X-ray sources and their optical counterparts divided by σ_x and the expected Rayleigh distribution (solid red curve) in W-CDF-S (top) and ELAIS-S1 (bottom). The solid blue curve represents the kernel density estimation of the normalized separation distribution. The agreement between the two distributions indicates that our empirically derived σ_x values are reliable.

the 68% positional uncertainty radius ($r_{68\%}$) and the number of source counts:

$$\log_{10} r_{68\%} = \alpha \times \log_{10} C + \beta. \quad (2)$$

Following Chen et al. (2018), we define σ_x to be the same as the uncertainties in R.A. and decl. ($\sigma_{\rm R.A.} = \sigma_{\rm decl.} = \sigma_x$), so that $\sigma_x = r_{68\%}/1.515$ (see Pineau et al. 2017 for details). With the updated σ_x, we run NWAY again, iterating until the α and β values become stable.

The distribution of σ_x can be roughly approximated as a normal distribution. For the W-CDF-S field, the average σ_x in the full/soft/hard band is $1\farcs15/1\farcs25/1\farcs10$, with a standard deviation of $0\farcs46/0\farcs51/0\farcs31$. For the ELAIS-S1 field, the average σ_x in the full/soft/hard band is $1\farcs15/1\farcs21/1\farcs15$, with a standard deviation of $0\farcs51/0\farcs55/0\farcs34$. Since we assume $\sigma_{\rm R.A.} = \sigma_{\rm decl.} = \sigma_x$, the separation between X-ray sources and their optical counterparts should follow the Rayleigh distribution (with the scaling parameter σ_x). The distribution of the normalized separation (Separation/σ_x) between the full-band X-ray sources and their optical counterparts is presented in Figure 8, along with the Rayleigh distribution. The good agreement between the distribution of separation/σ_x and the Rayleigh distribution indicates that our empirically derived σ_x values are reliable indicators of the true positional uncertainties.

3.5. The X-Ray Source Catalogs

We present the schema of the X-ray source catalogs for the W-CDF-S and ELAIS-S1 fields in Appendix A. With the DET_ML thresholds derived in Section 3.3, we detect 3512/3672/1118 sources in the full/soft/hard band in the W-CDF-S field, and 2328/2342/884 sources in the full/soft/hard band in the ELAIS-S1 field. These numbers only include pointlike sources; sources that have $\geqslant$10 improvements in the detection likelihood when detected as an extended source compared to the likelihood when detected as a pointlike source are not included in our X-ray catalogs. To combine sources detected in the three energy bands, we first need to identify sources that are detected in more than one band. Two sources detected in different bands are considered to be the same if their angular separation is smaller than 10″, or the quadratic sum of the 99.73% positional uncertainties from both bands. Then, we add sources that are only detected in a single band to the source list. We thus have a catalog of 4053/2630 unique pointlike sources (see Figure 9 for the spatial distribution of sources) in the

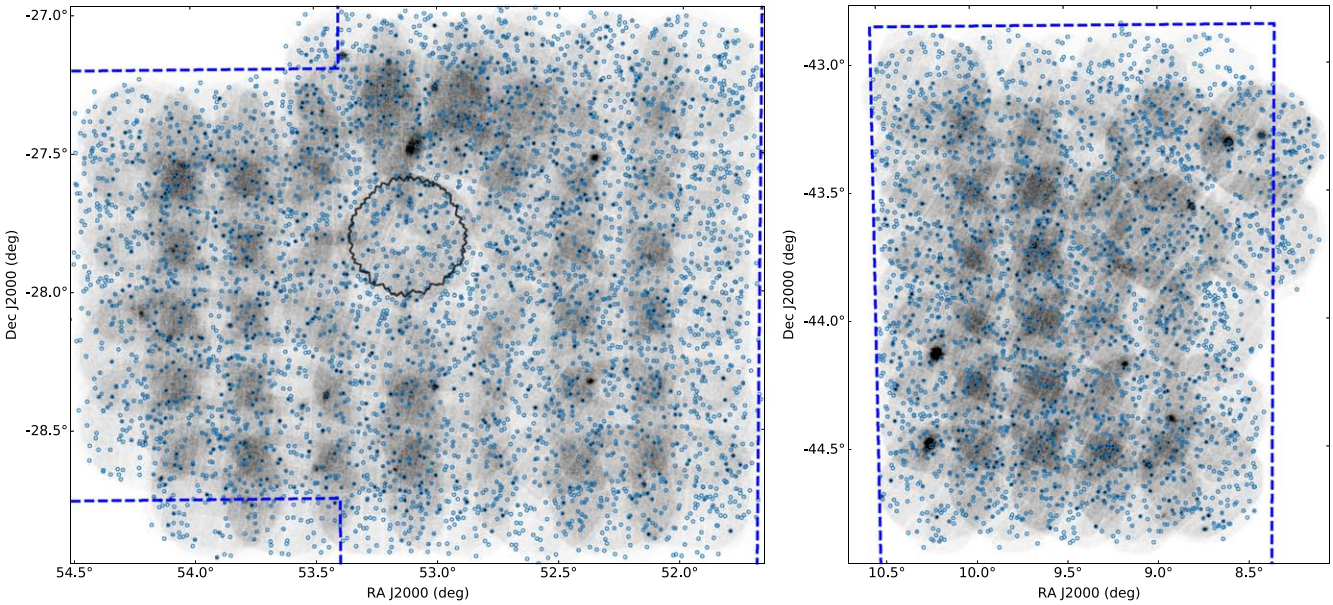

Figure 9. Left: spatial distribution of the pointlike X-ray-detected sources in the W-CDF-S field (blue circles) projected on the smoothed full-band image. The blue dashed line encloses the region with forced optical-NIR photometry (K. Nyland et al. 2021, in preparation). The black solid curve indicates the footprint of the 7 Ms CDF-S (Luo et al. 2017). W-CDF-S is larger than the CDF-S by a factor of ≈34 in solid angle. Right panel: spatial distribution of the pointlike X-ray-detected sources in the ELAIS-S1 field (blue circles) projected on the smoothed full-band image. The blue dashed line encloses the region with forced optical-NIR photometry (Zou et al. 2021).

W-CDF-S/ELAIS-S1 field. In the W-CDF-S/ELAIS-S1 field, a total of 2262/1407 sources have more than 100 PN+MOS counts in the full band; 139/78 sources have more than 1000 X-ray counts in the full band (see Figure 11 for the counts distribution). For the W-CDF-S field, ≈5/12/1% of the sources are only detected in the full/soft/hard band; for the ELAIS-S1 field, ≈5/10/1% of the sources are only detected in the full/soft/hard band. We have performed visual examinations to ensure that no obvious sources are missing from the catalogs, and that there are no obvious false matches between different bands.

When a source is not detected in all the bands, we estimated its count-rate upper limits in bands where the source is undetected. The minimum required source counts (m) for a source to be detected with the `emldetect` detection threshold ($P_{\rm random}$; `det_ml` $= -\ln P_{\rm random}$) at a given number of background counts (B) can be estimated by solving the following regularized upper incomplete Γ function (Chen et al. 2018):

$$P_{\rm Random} = \frac{1}{\Gamma(m)} \int_B^{\infty} t^{m-1} e^{-t} dt. \quad (3)$$

Here, B is estimated by summing the number of counts in 5×5 pixels centered at the source position in the mosaicked background map. We note that the estimated m corresponds to the Poisson detection likelihood of $P_{\rm Random}$, which is not necessarily equal to the detection likelihood from PSF fitting in EMLDETECT. However, as the PSF fitting likelihood follows a 1:1 relation with the Poisson likelihood in general (Liu et al. 2020), our estimation roughly holds. With the estimated m, the count-rate upper limit is then calculated with the formula:

$$\mathrm{RATE}_{\rm upper\ limit} = \frac{m - B}{t_{\rm exp} \times \mathrm{EEF}}, \quad (4)$$

where $t_{\rm exp}$ represents the exposure time at the source position, and the encircled energy fraction (EEF) value corresponding to the 5×5 pixels centered at the source position is obtained from the EEF map. To derive the EEF map, we use `psfgen` to generate a series of PSF models for the three EPIC cameras, with different off-axis angles and different energies. These PSF models approximate the EEF as a function of the off-axis angle for different EPIC cameras at different energies. For each observation, an EEF map is generated for each EPIC camera. A mosaicked EEF map for different EPIC instruments at different energies is constructed (see Figure 10 for the soft-band EEF maps). The EEF value adopted in Equation 4 is the weighted EEF of EEF values at the source position for the three EPIC cameras, with the counts number in the band where the source is detected in each EPIC camera serving as the weight. Similarly, as exposure times in different EPIC cameras vary, the $t_{\rm exp}$ adopted in Equation 4 is the weighted $t_{\rm exp}$ (with the same weights as those utilized to calculate the weighted EEF).

To convert the count rate to flux, we derive the effective power-law photon indices, $\Gamma_{\rm eff}$ (or the upper/lower limits of the indices), for X-ray sources from the hard-to-soft-band ratios (or the lower/upper limits of the band ratios), assuming a power law modified by Galactic absorption. The band ratio is calculated as the ratio between the hard-band count rate and the soft-band count rate. The relation between the band ratio and $\Gamma_{\rm eff}$ is derived from the canned response files of EPIC cameras.[45] The soft/hard/full-band flux of the source is derived from the soft/hard/full-band count rate in each EPIC camera assuming a power-law spectrum with the derived $\Gamma_{\rm eff}$; the weighted mean of fluxes obtained from all available EPIC cameras (the ratio between the count rate and the count-rate error in each camera is utilized as the weight) is reported as the flux of the source. For sources that are detected in the soft band but not in the hard band in W-CDF-S and ELAIS-S1, we stack their hard-band counts at the source positions to derive a stacked $\Gamma_{\rm eff}$, which is ≈1.9 in W-CDF-S and ≈2.0 in ELAIS-S1. The stacking is performed

[45] https://www.cosmos.esa.int/web/xmm-Newton/epic-response-files